ROYAL SOCIETY
OF CHEMISTRY

Check for updates

Anti-naphthalene bisbenzimidazole columnar mesogens as interfacial modifiers in perovskite solar cells

Ankita Sharma, [a] Paresh Kumar Behera, †[b] Kajal Yadav,[a] Tarun, [a]
Pankaj Yadav,[c] Achalkumar Ammathnadu Sudhakar *[bd] and
Upendra Kumar Pandey *[a]

Introducing an interfacial layer is a strategic way to improve the performance and stability of perovskite solar cells by optimizing charge transport, reducing recombination, and enabling proper energy level alignment. In conventional perovskite solar cells, the commonly used hole transport layer, spiro-OMeTAD, is limited by its poor hole mobility, low intrinsic conductivity and susceptibility, which result in interfacial defects and device degradation. To address these challenges, we developed organically self-assembled semiconductors utilizing anti-naphthalene bisbenzimidazole (**NB20**) as an interfacial layer between the perovskite and spiro-OMeTAD. The **NB20** layer enhances hole extraction, passivates the interfacial defects, and improves charge transport, leading to an approximately 9% performance boost through better energy level alignment and lower recombination losses. Additionally, the modified device with the passivated layer shows enhanced stability by maintaining 80.69% of its original power conversion efficiency after 1000 hours, whereas unmodified devices have retained only 58.73% of their initial performance.

1. Introduction

The demand for efficient and cost-effective solar energy solutions has led to continuous changes in photovoltaic technologies, starting with first-generation silicon-based solar cells that are more flexible but restricted by high manufacturing costs and structural rigidity. Second-generation thin-film technologies have emerged as an alternative, but their efficiency remained lower than that of silicon-based cells. Ultimately, the third-generation, perovskite solar cells (PSCs) were introduced as leading candidates for the future of solar energy owing to their excellent efficiency and simple fabrication process.[1] The concept of perovskite solar cells was first demonstrated in 2009 by Miyasaka et al.,[2] when they successfully fabricated a solar cell using $CH_3NH_3PbI_3$, a material that exhibited remarkable photovoltaic properties. The PSC efficiency improved from 3.8% (2009) to 27.0% (2025) due to advancements in material composition, deposition techniques, interface engineering and bulk engineering.[3] The key to this high performance lies in the structure of perovskites, which is denoted using the formula ABX_3, consisting of three components: an A-site cation, a B-site cation, and X-site anions. The A-site is typically filled with a larger organic cation (like methylammonium (MA^+) or formamidinium (FA^+)) or an inorganic cesium (Cs^+) ion. The B-site contains a smaller metal ion, commonly tin (Sn^{2+}) or lead (Pb^{2+}), which is responsible for the material's electronic properties. The X-site typically includes halide anions, for example, iodide (I^-), bromide (Br^-), or chloride (Cl^-), which bridge the metal cations and influence the charge transport properties of the material.[4] The ABX_3 structure has been optimized to enhance the efficiency and stability of PSCs. Early formulations such as $MAPbI_3$ and $FAPbI_3$ achieved high power conversion efficiencies (PCEs) but suffered from significant thermal and structural instability. To address these challenges, mixed-cation and mixed-halide compositions have emerged. One of most extensively studied and highly efficient formulations is $Cs_{0.05}(FA_{0.79}MA_{0.16})_{0.95}Pb(I_{0.77}Br_{0.23})_3$, where cesium, formamidinium, and methylammonium cations mix at the A-site, and the X-site is a blend of iodide and bromide anions.

[a] Organic & Flexible Electronics Laboratory, Department of Electrical Engineering, School of Engineering, Shiv Nadar Institution of Eminence, G.B. Nagar, Uttar Pradesh-201314, India. E-mail: upendra.pandey@snu.edu.in

[b] Department of Chemistry, Indian Institute of Technology Guwahati, Guwahati, Assam-781039, India. E-mail: achalkumar@iitg.ac.in

[c] Department of Solar Energy, School of Technology, Pandit Deendayal Energy University, Gandhinagar, Gujarat-382 007, India

[d] Centre for Sustainable Polymers, Indian Institute of Technology Guwahati, Guwahati, Assam-781039, India

† Present address: Department of Chemistry, University of Oxford, Mansfield Road, Oxford, OX13TA, UK.

This composition enhances thermal stability and film quality, leading to more durable and efficient devices.[5] Various device architectures have been proposed to achieve high performance, including both mesoscopic and planar geometries, with configurations based on either p–i–n or n–i–p structures.[6] The n–i–p configuration is commonly used in PSCs due to its optimized charge transport and improved stability. The structure comprises of an electron transport layer (ETL, n-type), an intrinsic light-absorbing perovskite layer, and a hole transport layer (HTL, p-type).[7] In this configuration, electrons are extracted through the ETL, whereas the HTL assists in hole extraction. Despite its advantages, this structure faces several issues that restrict its sustained performance over time. One of the main challenges with spiro-OMeTAD as a HTL is its inherently low conductivity and poor hole mobility, typically ranging from $\sim 10^{-8}$ to 10^{-6} cm^2 V^{-1} s^{-1}.[8] To enhance its conductivity and mobility, p-type additives like lithium bis(trifluoromethanesulfonyl)imide (LiTFSI), 4-*tert*-butylpyridine (TBP) and tris(2-(1*H*-pyrazol-1-yl)-4-*tert*-butylpyridine)cobalt(III)bis(trifluoromethanesulfonyl)imide (FK 209 Co(III) TFSI) are introduced into spiro-OMeTAD. However, doping with LiTFSI and TBP creates charge traps at the interface between the perovskite and HTL, resulting in increased recombination losses and reduced efficiency.[9] Similarly, FK20 can cause poor adhesion and high impedance at the interface, which obstructs effective charge carrier extraction and may adversely affect device stability.[10] Thus, it reduces the device performance and its longevity.

In response to these challenges, interfacial engineering is crucial in boosting the PSC performance and stability, which involves modification of the perovskite/HTL interfaces to optimize charge carrier extraction kinetics, reduce losses through grain boundary passivation, and passivate the defects.[11] One of the prime strategies is the use of columnar self-assembled organic semiconductors broadly recognized as discotic liquid crystals (DLCs). DLC materials include an aromatic core at the centre, functionalized with flexible alkyl group side chains and linkers. In this study we have utilized an *anti*-naphthalene bisbenzimidazole (**NB20**) based DLC showing ambipolar charge carrier transport as an interlayer between the perovskite and the hole transporting layer in PSCs. Behera *et al.* have shown that **NB20** exhibits electron and hole mobility values of 1.92 × 10^{-3} cm^2 V^{-1} s^{-1} and 2.22 × 10^{-3} cm^2 V^{-1} s^{-1} respectively, without the use of dopants typically required for widely used HTL materials in perovskite solar cells such as spiro-OMeTAD.[12] It is to be noted that **NB20** cannot operate as a pure HTL because its ambipolar nature does not provide the required electron blocking function, but its high mobility is expected to enhance charge transport between the perovskite and spiro-OMeTAD, assisting in achieving better charge separation.[12–14] Moreover, **NB20** provides a favourable HOMO energy level, which aligns well with the valence band maximum of the perovskite absorber and spiro-OMeTAD. A proper energy level alignment reduces energy losses and suppresses non-radiative recombination, key factors contributing to poor device performance. Additionally, **NB20** with its planar π-conjugated core and electron-withdrawing carbonyl groups exhibits strong

π–π interactions that drive cofacial head-to-head stacking.[12] This arrangement facilitates the formation of H-aggregates, characterized by parallel chromophore alignment, leading to better absorption.[15] **NB20** provides excellent chemical stability along with moisture and oxygen resistance, expected to protect the underlying perovskite layer from degradation at the interfaces under environmental stress.[4] Moreover, columnar mesogens are known to self-heal over a period of time and improve charge transport.[16]

2. Experimental details

Materials

The perovskite precursor materials, formamidinium iodide (FAI) and methylammonium bromide (MABr), were sourced from Great cell Solar Materials. Lead(II) iodide (PbI$_2$), spiro-OMeTAD, lead(II) bromide (PbBr$_2$) and cesium iodide (CsI) were sourced from TCI. Titanium diisopropoxide bis (acetylacetonate), acetonitrile (ACN), dimethylformamide (DMF), chlorobenzene, dimethyl sulfoxide (DMSO), FK209 CO(III) TFSI salt, bis(trifluoro methane) sulfonamide lithium salt, and 4-*tert*-butylpyridine were acquired from Sigma Aldrich. Tin(IV) oxide (15%) in H$_2$O colloidal dispersion was received from Thermo Scientific and titanium tetrachloride (TiCl$_4$) was received from Spectrochem. All chemicals were used without additional purification.

Fabrication

The device configuration of the perovskite solar cell, *i.e.*, FTO/c-TiO$_2$/SnO$_2$/Cs$_{0.05}$(FA$_{0.79}$MA$_{0.16}$)$_{0.95}$Pb(I$_{0.77}$Br$_{0.23}$)$_3$/**NB20**/spiro-OMeTAD/Au is presented in Fig. 1(a). First, FTO (fluorine-doped tin oxide, 7 Ω cm^{-2}, Xinjiang Technologies, Hongkong, https://en.wikipedia.org/wiki/Xinjiang) coated glass substrates (2.5 cm^2) are cleaned in an ultrasonic bath using soap solution (Hellmanex III, Sigma-Aldrich), deionized water, acetone, and isopropanol for 30 minutes each, at 50 °C for 15 minutes to remove any residual contaminants. Next, c-TiO$_2$ is prepared by dissolving titanium diisopropoxide bis(acetylacetonate) (100 µL) and 2 M HCl (7 µL) in EtOH (1.0 mL), followed by spin-deposition of the formulation over the FTO substrate at 6000 rpm for 40 seconds. Then the coated substrate was tempered at 500 °C for 1 hour. Afterward, the c-TiO$_2$ layer was exposed to 40 mM TiCl$_4$ at 75 °C for 20 minutes and subsequently thermally treated for 40 minutes at 500 °C. Next, the SnO$_2$ layer is deposited by diluting a 15% colloidal SnO$_2$ dispersion in DI water at a 1:4 wt% ratio and spin-deposited at 3000 rpm for 30 seconds, followed by annealing for 30 minutes at 150 °C. The bilayer ETL has a thickness of ~40 nm. For deposition of the perovskite, the ETL coated substrate was immediately shifted to the nitrogen-purged glovebox (H$_2$O < 1 ppm, O$_2$ < 50 ppm). The perovskite solution was prepared according to our previously reported work.[17] Following this, the **NB20** interlayer is prepared by dissolving **NB20** in toluene, and the solution is applied upon the perovskite layer (4000 rpm for 30 seconds) followed by annealing at 70 °C for 3 min. Then, the HTL is prepared through dissolving spiro-OMeTAD (90 mg) in
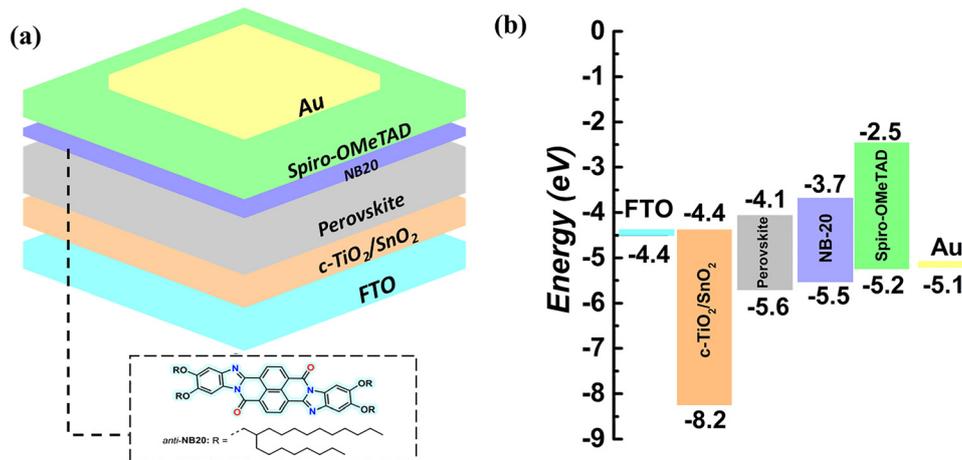
Fig. 1 (a) Perovskite solar cell schematic with **NB20** as an interfacial layer structure and (b) energy level alignment across layers.

chlorobenzene (1 mL). To this solution, 22 μL of Li-TFSI solution (520 mg of Li-TFSI in 1 mL of ACN), 36 μL of TBP, and 20 μL of FK20 solution (300 mg of FK209 in 1 mL of ACN) are added and stirred. The solution is then coated onto the **NB20** interlayer at 3000 rpm for 30 seconds. The thickness of the spiro-OMeTAD layer was measured using profilometry and found to be approximately 195 nm. Upon incorporation of **NB20**, the thickness increased slightly to ∼203 nm, resulting in a difference of about 8 nm, as shown in Fig. S1. After HTL deposition, the device was kept for aging inside the glove box at a controlled environment humidity level of ≤1%. Thereafter, gold (Au) electrodes were thermally evaporated under a 10^{-6} bar vacuum, achieving an active area of 9.9 mm^2, and the samples were aged again for a period of 20 hours before measurement.

Characterization

The ultraviolet-visible spectroscopy (UV-vis) spectrophotometer from Shimadzu, SolidSpec-3700 system, was utilized to study the absorption spectrum of films. To study the surface morphology of films, an FE-SEM (field emission scanning electron microscope) from JEOL, JEM-7001F, was utilized. X-ray diffraction spectroscopy (XRD) was carried out using a Bruker D8 Discover lab-scale X-ray diffractometer with a Cu Kα radiation source (excitation wavelength: 0.154 nm). The steady state photoluminescence (PL) spectra were measured using a Horiba Fluorolog-3 spectrofluorometer with a 450 nm excitation wavelength. The time-resolved photoluminescence (TRPL) measurements were carried out using a Life spec II, Edinburgh Instruments. The current–voltage (J–V) measurement of the device was done using a Sciencetech solar simulator (AM1.5G), under one sun illumination using a Keithley 2450 source meter having a device active area of 0.099 cm^2. The contact angle of the film was measured using a Drop Shape Analyzer (KRÜSS, Hamburg, Germany). The thickness of the layers was determined using a Bruker Dektak XT surface profilometer. Electrochemical impedance (EIS) was performed using a KEYSIGTH Impedance Analyzer E4990A.

3. Results and discussion

The sustainability of the **NB20** interlayer in enhancing device performance, when used in PSCs, was first evaluated through energy level alignment studies, as depicted in Fig. 1(b). **NB20** was integrated between the perovskite layer and spiro-OMeTAD, where its −3.7 eV LUMO (lowest unoccupied molecular orbital) and −5.5 eV HOMO (highest occupied molecular orbital)[12] create a favourable alignment with the perovskite valence band (∼−5.6 eV) and the spiro-OMeTAD HOMO (∼−5.2 eV). This favourable energy alignment ensures smooth charge transfer and facilitates efficient hole extraction in the direction from the perovskite *via* **NB20** to spiro-OMeTAD, thereby minimizing interfacial barriers and suppressing non-radiative recombination losses.[18,19] The energy level values of the perovskite and spiro-OMeTAD were taken from ref. 8 and 5, respectively, where they were determined using ultraviolet photoelectron spectroscopy (UPS) and cyclic voltammetry. The Au work function was taken from standard values reported in the literature,[20] determined by density functional theory (DFT) and validated with experimental photoelectron spectroscopy (PES) data. The FTO work function was cited from ref. 21, where it was directly measured using UPS, and the c-TiO$_2$/SnO$_2$ positions were similarly referenced from the literature.[17,22] Overall, this well-aligned energy landscape highlights the crucial role of **NB20** in enhancing the interfacial contact and facilitating efficient charge extraction.[23]

Furthermore, X-ray diffraction (XRD) analysis was carried out to identify the optimal **NB20** concentration and to verify that its incorporation as an interlayer does not adversely affect the intrinsic crystallographic features of the perovskite bulk layer. The fitted XRD patterns for all **NB20** concentrations used during optimization are provided in Fig. S2 and S3. Fig. 2(a) displays the XRD patterns of base perovskite films (without **NB20**) and the film incorporating the optimal **NB20** concentration of 1.5 mg mL^{-1}, both exhibiting distinct perovskite diffraction peaks at approximately 14°, 28°, and 32°, corresponding to the (110), (220), and (310) planes respectively.
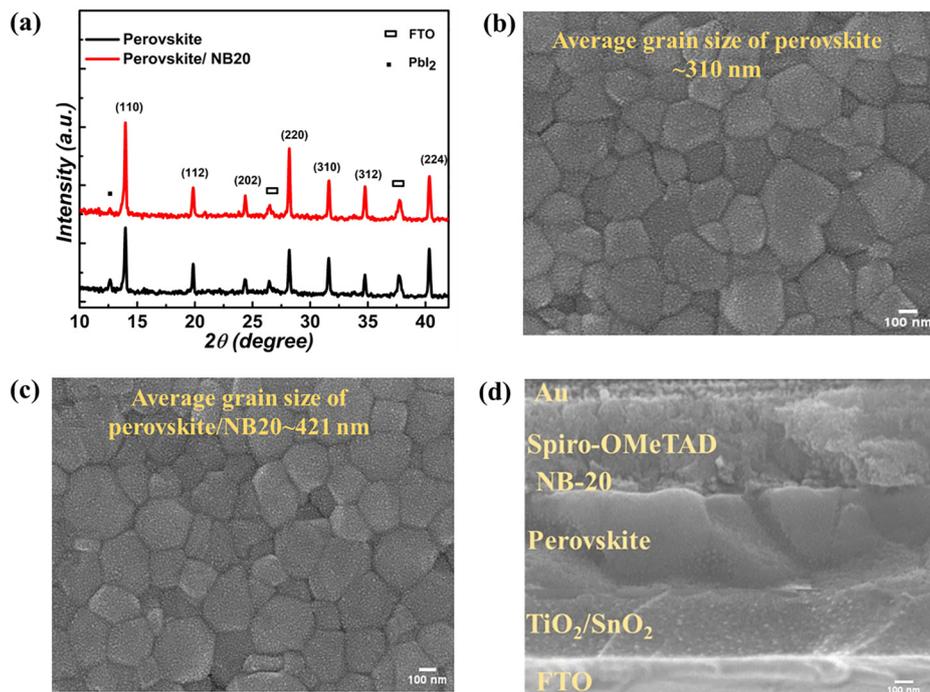
Fig. 2 (a) XRD patterns of perovskite films with and without the **NB20** interlayer. FE–SEM images of (b) the pristine perovskite film and (c) the **NB20**-treated perovskite film. (d) Cross-sectional SEM image illustrating the layered architecture of the complete device.

Upon incorporation of the **NB20** interlayer, the XRD patterns show no emergence of new diffraction peaks or noticeable shifts in the existing ones, confirming that the intrinsic crystal structure of the perovskite remains unaltered. This suggests that **NB20** does not penetrate the bulk perovskite but rather localizes at the surface and grain boundaries of the perovskite layer. Furthermore, the base perovskite exhibited a FWHM (full width at half maximum) of 0.193 and peak intensity of 104.22, whereas the 1.5 mg mL^{-1} **NB20** interlayer demonstrated the most favourable results, achieving a FWHM of 0.180 and the highest XRD peak intensity of 149.89. This combination of narrower peak width and increased intensity indicates improved surface quality with reduced grain boundaries (crystallinity) in the presence of the **NB20** interlayer. This may be attributed to the planar π-conjugated naphthalene-bis(benzimidazole) core of **NB20**, facilitating strong π–π stacking interactions, promoting ordered molecular alignment and inducing suppressed grain boundaries.[24,25] Notably, the base perovskite film shows a distinct PbI$_2$ diffraction peak at 12°, indicating the presence of unreacted PbI$_2$ on the surface. In contrast, the **NB20** treated sample exhibits a slightly reduced PbI$_2$ peak. This improvement is attributed to the coordination interaction between the benzimidazole nitrogen atoms of **NB20** and the undercoordinated Pb^{2+} ions present at the perovskite surface.[26] Such Pb–N coordination effectively passivates surface defects present in the base perovskite.[27]

Moreover, the surface morphology of perovskite films with and without the **NB20** interlayer was examined using field emission scanning electron microscopy (FESEM). The top-view FESEM images of the base perovskite (Fig. 2b) and the

perovskite with **NB20** (Fig. 2c) reveal differences in grain connectivity. The corresponding grain-size distribution histograms derived from these images depicted in Fig. S4 show that introducing the **NB20** interlayer increases the average grain size from ∼310 nm in the base film to ∼421 nm in the **NB20** film. This enhancement can be attributed to the **NB20** induced surface passivation, which occurs due to the process of recrystallization. This suggest that **NB20** preferentially deposits at the surface and/or grain boundaries of the perovskite layer, effectively passivating defect sites. Such defect suppression reduces charge recombination and contributes to the formation of a higher quality perovskite film, thereby facilitating more efficient charge transport across the device layers.[28] Additionally, the SEM images of perovskite films prepared with different **NB20** concentrations (Fig. S4) show that higher **NB20** loadings negatively affect the film morphology. This confirms that the amount of **NB20** must be carefully optimized. Based on the combined XRD (Fig. S2) and SEM (Fig. S4) analyses, the 1.5 mg mL^{-1} **NB20** concentration provides the most balanced and uniform film quality, making it the optimal interlayer condition, and the results confirm that **NB20** predominantly interacts with the surface and grain boundary regions rather than altering the perovskite bulk layer.[29,30] Accordingly, Fig. 2(d) presents the cross-sectional image of the complete device stack, confirming uniform film growth and good interfacial contact between the different layers. A well-defined interface is necessary for the improvement in charge separation and movement within the device.[31,32]

Furthermore, the optical behaviour of the perovskite with and without the **NB20** interlayer was investigated using UV-vis

absorption spectroscopy. Fig. S5 depicts that the perovskite treated with a thin layer of **NB20** shows an absorption profile similar to that of the base perovskite, confirming that the interlayer does not affect the intrinsic optical properties of the perovskite. However, a slight enhancement in the absorption of the ultrathin film stack is observed in the 450–550 nm region, resulting from the broad visible absorption of the **NB20** molecule as well as optimized optical interference conditions (reduced surface scattering) within the ultrathin film stack of the perovskite and **NB20**.[33] Beyond 550 nm, both films exhibit a characteristic gradual decrease in absorption associated with the band-edge region of the perovskite. The absence of any noticeable change in this region further confirms that the **NB20** interlayer does not change the bulk optical properties of the perovskite absorber. Furthermore, no significant change in the bandgap of the perovskite in the presence of the **NB20** interlayer was observed (Fig. S6), indicating insignificant modification to the electronic structure of the perovskite bulk layer.[34] Consequently, the moderate enhancements observed after introducing the thin **NB20** interlayer supported by XRD, UV-Vis, and FE-SEM analyses confirm that **NB20** functions as an effective interfacial passivation layer. This behaviour is consistent with previously reported surface-passivation strategies, where the modifying molecule primarily interacts with the surface and grain-boundary regions rather than altering the bulk perovskite lattice itself.[26,27,35–38]

To study charge carrier behaviour, steady state PL and transient TRPL analyses were performed. Fig. 3(a) presents the PL spectra of perovskite films with and without the **NB20** interlayer, highlighting the influence of **NB20** when inserted between the perovskite and the HTL. The PL intensity quenching of the **NB20** film is stronger compared to that without the **NB20** film, demonstrating that the presence of the interlayer results in better charge extraction from the perovskite to spiro-OMeTAD.[39,40] Similarly, TRPL measurements were conducted, as presented in Fig. 3(b), for films with and without the **NB20** interlayer. The recorded TRPL spectra were fitted by applying a double exponential decay model, represented in eqn (1), and to calculate the average carrier lifetime τ_{avg}, eqn (2)[17,41] was used.

$$I(t) = I_O + A_1 \exp^{\frac{-t}{\tau_1}} + A_2 \exp^{\frac{-t}{\tau_2}} \tag{1}$$

$$\tau_{avg} = (A_1\tau_1^2 + A_2\tau_2^2)/A_1\tau_1 + A_2\tau_2) \tag{2}$$

Here, τ_1 represents a fast decay component, τ_2 a slower decay component, and t is the time variable. The amplitudes A_1, and A_2 correspond to the relative contributions of these decay processes.

The calculated τ_{avg} from the TRPL measurements shows a noticeable difference between perovskite films with and without the **NB20** interlayer. With the **NB20** layer, the τ_{avg} is 10.00 ns, which is shorter compared to that of the 23.68 ns film
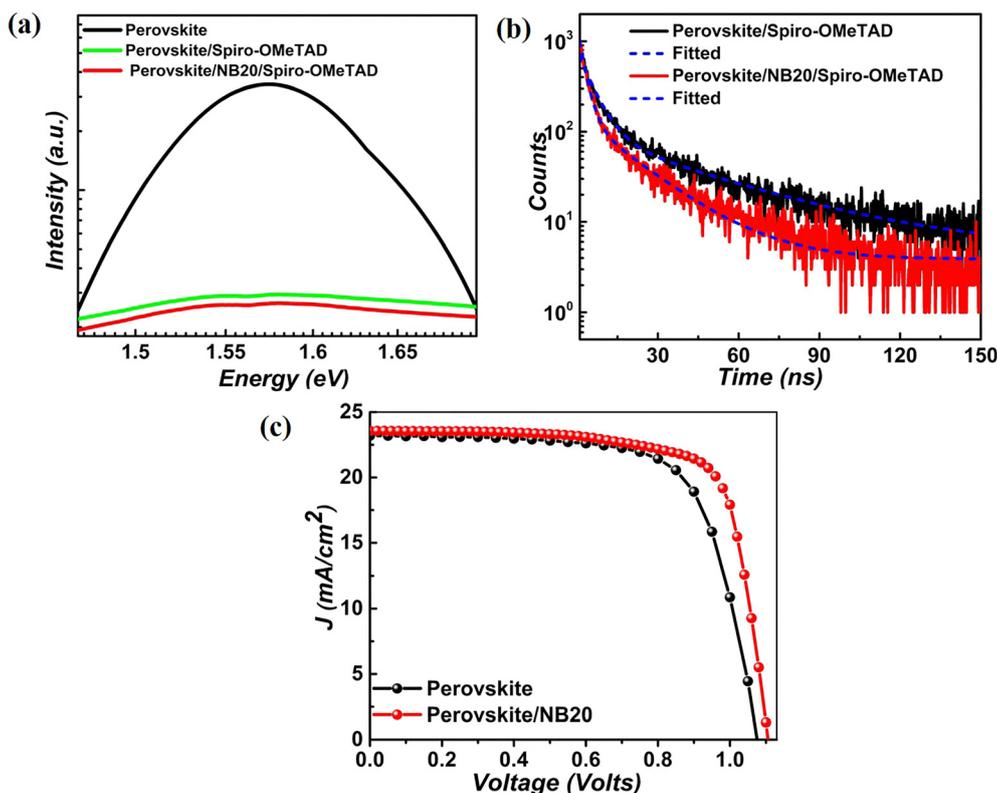

Fig. 3 (a) PL spectra demonstrating the effect of the **NB20** passivation layer between perovskite films and the HTL, (b) TRPL spectra demonstrating charge carrier dynamics with and without the interlayer and (c) the J–V plot of base and **NB20** passivated PSCs.

without **NB20**. This reduction in lifetime indicates that **NB20** effectively reduces trap-assisted recombination and enhances charge transport.[42,43] The detailed carrier lifetime data are summarized in Table S1 and Fig. S7.

Furthermore, for characterization of the solar cell performance, J–V measurements under 1 sun of AM 1.5G illumination were carried out. These measurements provide key device parameters, such as open circuit voltage (V_{oc}), short-circuit current density (J_{sc}), PCE and fill factor (FF). Fig. 3(c) shows the J–V curve, along with the data summarized in Table 1, which displays average performance parameters obtained from 15 devices, as well as the results of the champion device, for both with and without **NB20** configurations. Similarly, Table S2 summarizes the device performance at various concentrations of PCE across 15 devices, while Fig. S8 displays the respective J–V characteristics. The base device as a reference exhibits a V_{oc} of 1.08 V, J_{sc} of 23.20 mA cm^{-2}, FF of 0.70, and a PCE of 17.48%. Addition of 0.5 mg mL^{-1} of **NB20** resulted in a minimal enhancement in V_{oc} (1.11 V) and PCE (17.85%), indicating that **NB20** passivates defects and modifies the interface. Increasing the concentration to 1.5 mg mL^{-1} of **NB20** gave better results as V_{oc} improved to 1.12 V, J_{sc} enhanced to 23.59 mA cm^{-2}, FF rose to 0.72, and PCE reached its highest value of 19.02%. This enhancement indicates better defect passivation in the presence of **NB20**.[44] Importantly, improved J_{sc} and V_{oc} implies better suppression of carrier recombination, while the enhanced FF indicates improved charge transport dynamics within the device, as supported by PL and TRPL data. However, **NB20** concentration was when raised to 2.5 mg mL^{-1}, a decline in performance was recorded, with V_{oc} decreasing to 1.07 V, J_{sc} dropping to 23.00 mA cm^{-2}, FF remaining at 0.70, and PCE reducing to 16.93%. This indicates that beyond an optimal concentration, excessive **NB20** incorporation may lead to undesirable morphological changes (supported by SEM Fig. S4), leading to inefficient carrier extraction.[45] Additionally, Fig. 4 presents the statistical analysis of performance parameters for various concentrations of the passivation layer, revealing that **NB20** contributes to improving PSC efficiency within a specific concentration range, and the histogram in Fig. S10 illustrates the distribution of PCE across 15 devices. Both Fig. 4 and Fig. S10 together reveal batch-to-batch consistency and reproducibility. Based on the above observation, it was noted that the optimal performance was achieved at 1.5 mg mL^{-1}, achieving an optimal balance between recombination suppression and charge carrier mobility.[46] Beyond this concentration, material interaction creates a negative impact on perovskite layer uniformity, leading to performance degradation.[47] Therefore, controlling the concentration of **NB20** is essential to maximizing device performance. Additionally, the reason **NB20** is employed

as an interlayer rather than a standalone HTL is clearly illustrated by the data in Fig. S9 and Table S3. When used as a standalone HTL, **NB20** yields a significantly low PCE of only ~1%, highlighting its poor hole extraction capability. In addition, its ambipolar nature does not provide the required electron-blocking function, making it unsuitable as an effective standalone HTL. In contrast, when used as an interfacial modification layer, **NB20** effectively improves interface quality, reduces interfacial defects and enhances overall device performance.

Furthermore, for evaluating the dynamic reliability of solar cells hysteresis index (HI) measurement was done using eqn (3).[48]

$$HI = \frac{PCE_{reverse} - PCE_{forward}}{PCE_{reverse}} \quad (3)$$

Fig. 5(a) and (b) reveals that the HI of cells with **NB20** is 57.14% lower than the base cell, indicating a significant reduction in hysteresis (the HI values for different **NB20** concentrations are summarized in Table S4). This improvement in reduced HI is attributed to the ability of **NB20** to mitigate defects at the perovskite/HTL interface, reducing trap-assisted recombination and charge accumulation.[49–51] Overall, the **NB20** interlayer addition improves film morphology and reduces defects, resulting in more stable and efficient device performance.

The EIS experiments were conducted to determine the influence of **NB20** on charge recombination and transport in devices. Nyquist plots provide a visual representation of the impedance data, displaying the relation between real and imaginary components of impedance at various frequencies (Fig. 5(c)). The equivalent circuit model used to fit the EIS data is shown as an inset within the graph and is also depicted in Fig. S11 for clarity, with parameters such as R_s (series resistance), R_{ct} (charge transfer resistance), and R_{rec} (recombination resistance) summarized in Table S5. In the plot, the high-frequency region represents R_s, while the mid-to-low-frequency region represents recombination and charge transfer processes.[52] The semicircular arc in the Nyquist plot reflects R_{ct}, while the tail at the lower frequencies is associated with R_{rec}, which is directly linked to recombination at the interfaces and the efficiency of charge extraction. The EIS data reveal that the R_s and R_{ct} for devices with **NB20** are 141.1 Ω and 35225 Ω, compared to 143.1 Ω and 39947 Ω for the device without **NB20**, suggesting that the addition of **NB20** reduces the resistance, which facilitates more efficient charge transport through the device. More importantly, the R_{rec} is significantly higher for with **NB20** PSCs (183 727 Ω) compared to that (142 321 Ω) without **NB20**. This indicates that **NB20** treatment decreases charge recombination between the perovskite

Table 1 Overview of photovoltaic parameters for without and with passivated PSCs, with average values of 15 devices and the best-performing device (in brackets)

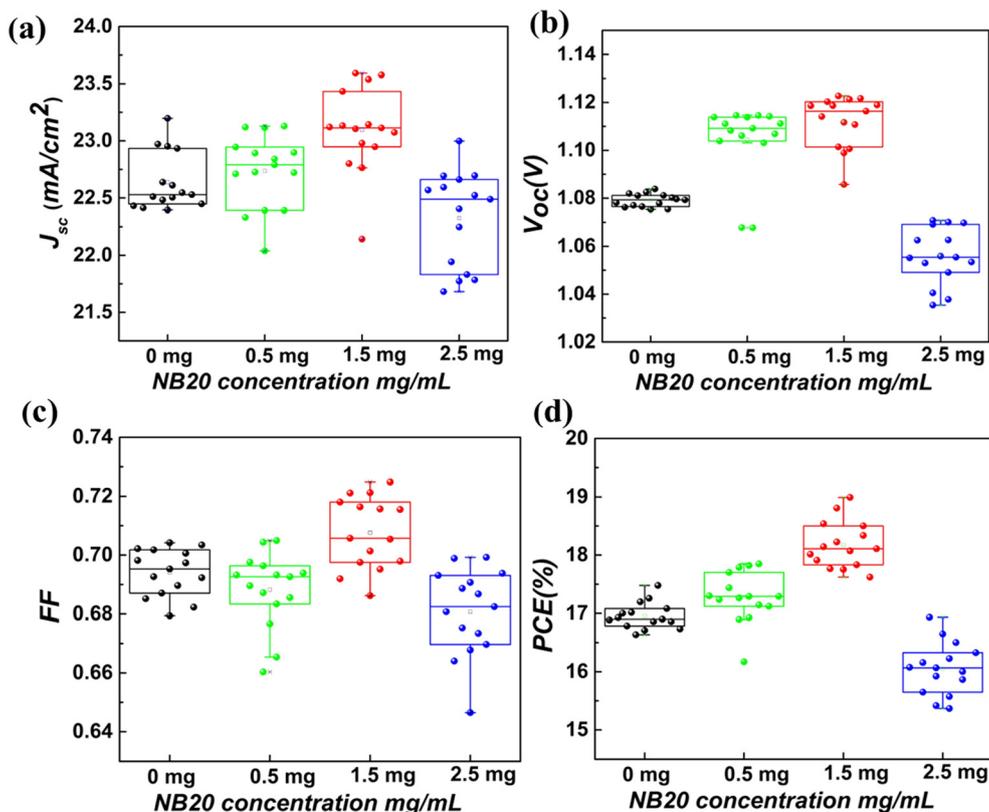| Device	J_{sc} (mA cm^{-2})	V_{oc} (V)	FF	PCE (%)
Perovskite	22.64 ± 0.25 (23.20)	1.08 ± 0.01 (1.08)	0.69 ± 0.01 (0.70)	16.96 ± 0.23 (17.48)
Perovskite/**NB20**	23.10 ± 0.37 (23.59)	1.11 ± 0.01 (1.12)	0.71 ± 0.01 (0.72)	18.18 ± 0.40 (19.02)

Fig. 4 Device statistics for different concentrations of the **NB20** layer: (a) J_{sc} (mA cm^{-2}), (b) V_{oc} (V), (c) FF and (d) PCE (%) of PSCs.

and spiro-OMeTAD interface, ensuring a reduction in the loss of charge carriers.[53,54] Additionally, the **NB20** passivated PSC exhibits a higher C_1 value (5.59 × 10^{-9} F) and a lower C_2 value (75.75 × 10^{-9} F) compared to the without **NB20** device (C_1 = 5.25 × 10^{-9} F, C_2 = 104.66 × 10^{-9} F), indicating improved interfacial charge transport and reduced recombination. The increase in C_1 arises from enhanced interfacial capacitance due to better charge accumulation and hole extraction at the perovskite/HTL interface, while the decrease in C_2 suggests a lower trap density and suppressed carrier recombination in the perovskite layer. Moreover, the **NB20** device exhibits a longer recombination lifetime of 10.3 × 10^{-4} sec compared to 7.48 × 10^{-4} sec for the base device. These overall results confirm that the **NB20** interlayer effectively facilitates charge transfer and passivates interfacial defects[37,38], further supporting the lower HI.[55] In order to further probe the improvement in the device performance, dark J–V characteristics were recorded, shown in Fig. 6(a). Dark J–V data duly supplement the observed EIS results by highlighting improvements in shunt resistance (R_{sh}), reduction in leakage current (J_0) and R_s in devices with **NB20** passivation as compared to those without **NB20**; increase in R_{sh} reduces power loss due to shunting, leading to higher FF and V_{oc}. This improvement indicates better charge collection and less energy loss. Additionally, the slight decrease in J_0 suggests fewer impurities and improved interface quality between layers. Similarly, a decrease in R_s minimizes contact resistance at the interface.[56]

To evaluate the influence of passivation on charge transport properties and defect trap density, dark space-charge limited current (SCLC) analyses were carried out. Hole mobility and defect trap density were evaluated in a hole-only device with the configuration (Fig. S12) ITO/PTAA/perovskite/spiro-OMeTAD/Au for the reference sample, while the passivated device incorporated an additional **NB20** layer ITO/PTAA/perovskite/**NB20**/spiro-OMeTAD/Au. For complete experimental details, please refer to SI, Section S10. The hole mobility was obtained by fitting the J–V characteristics (shown in Fig. S13) with the modified Mott–Gurney equation (eqn (4)),[57] while the defect trap density for both with and without the **NB20** passivation layer was calculated from the log–log J–V plot, presented in Fig. S14 using eqn (5)[58]

$$J = \frac{9}{8}\mu\varepsilon_r\varepsilon_o\frac{V^2}{d^3}\exp\left(0.891\gamma\sqrt{\frac{V}{d}}\right) \quad (4)$$

$$\eta_{trap} = \frac{2V_{TFL}\varepsilon_r\varepsilon_o}{qd^2} \quad (5)$$

Here, d represents thickness of the active region, q represents the fundamental charge, η_{trap} is the defect density, V_{TFL} denotes the trap filled limited voltage, ε_r (44)[59] denotes the material's relative dielectric constant, V denotes the applied voltage, ε_o is the permittivity of free space, J is the measured current density (sample 6.6 mm^2), γ symbolizes the fitting
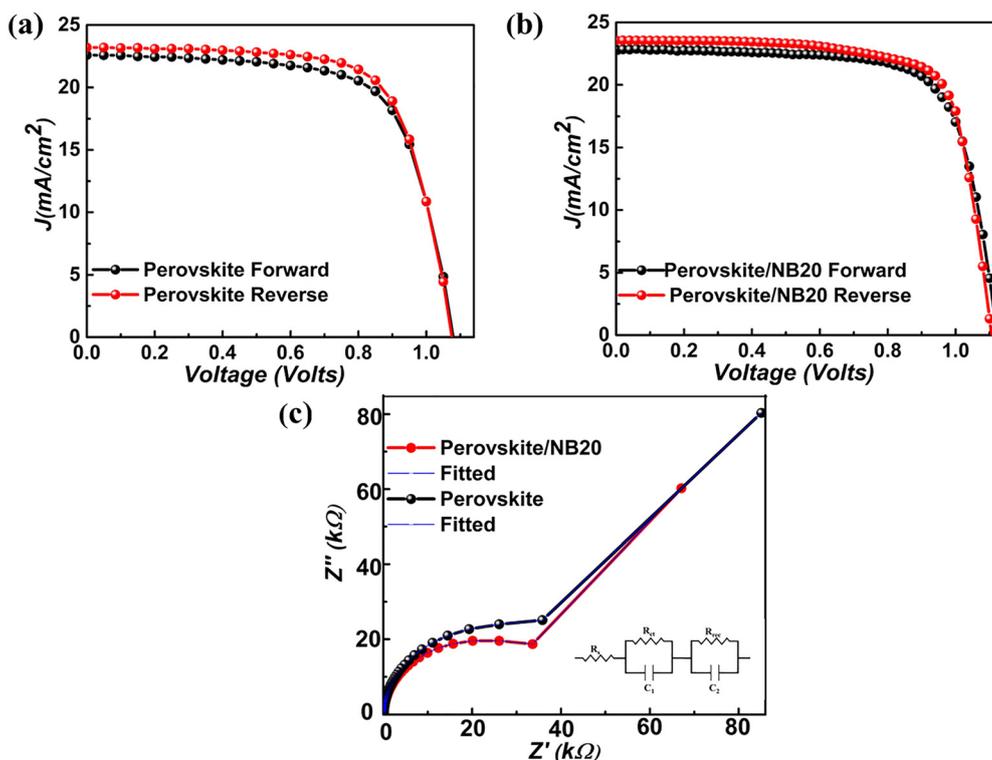
Fig. 5 *J*–*V* curves to calculate the hysteresis index (HI) of PSCs (a) without **NB20** and (b) with **NB20** and (c) Nyquist plots from EIS, comparing the impedance of devices; the equivalent circuit diagram used for fitting is shown as an inset within the graph.
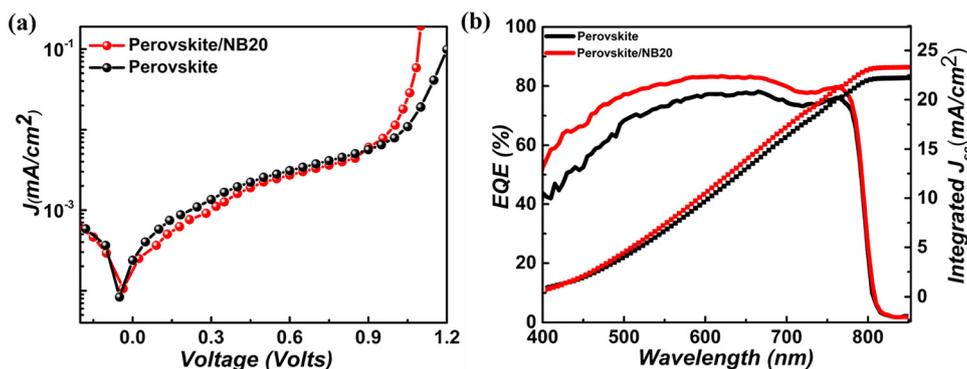

Fig. 6 (a) Dark *J*–*V* curves of base and **NB20** devices, highlighting the effect of passivation on PSCs, and (b) EQE spectral comparison of PSCs with and without the interlayer.

parameter that quantifies the intensity of the field dependence and μ represents the charge carrier mobility.[60]

The calculated hole mobility from the *J*–*V* curve of Fig. S13 for the device stack incorporating **NB20** was found to be 2.89×10^{-3} cm^2 V^{-1} s^{-1}, higher than the mobility of $1.57 \times$ cm^2 V^{-1} s^{-1} observed for base devices (without **NB20**). Furthermore, the defect density calculations, averaged over three best performing devices, are summarized in Table S6 and depicted in Fig. S14. An overall reduction of ∼14% in the trap density was observed in the **NB20** passivated devices compared to the reference device. This reduction in trap density may be

attributed to the effective passivation of buried interfaces, where trap-assisted recombination is predominantly governed by interfacial rather than bulk defects. Even modest reduction in trap density within the 10^{16} cm^{-3} range is shown to yield measurable improvements in V_{oc}, FF, and long-term device stability, owing to the exponential dependence of non-radiative recombination processes on defect density. This enhancement in observed hole mobility in device stack may be attributed to suppressed trap density along with improved interface duly supported by XRD and SEM measurements, leading to improved charge transport.[61,62] This substantial decrease in
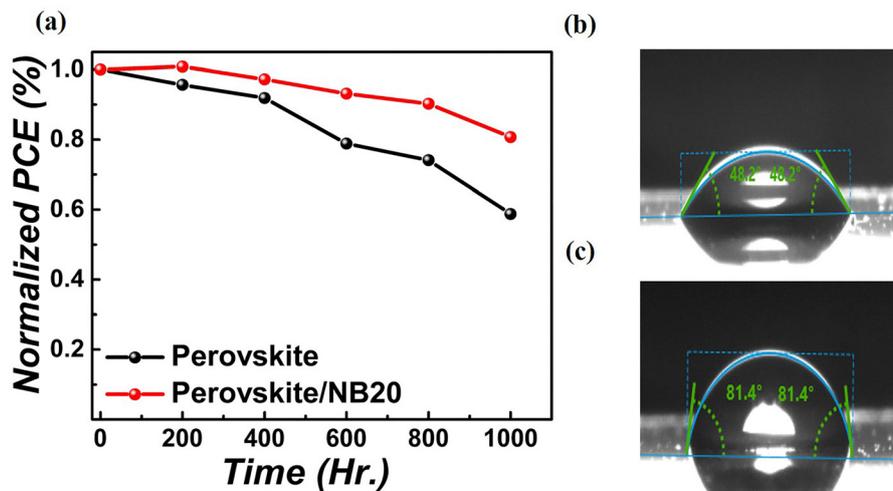
Fig. 7 (a) Normalized stability measurements for both treated and untreated **NB20** without the encapsulation device and contact angle measurements on (b) the perovskite film and (c) the **NB20** passivated film.

trap density confirms that **NB20** functions as an effective passivation layer.[25,63]

Moreover, as illustrated in Fig. 6(b), the EQE (external quantum efficiency) peak for cells incorporating **NB20** reaches approximately 80%, whereas those without **NB20** exhibit around 70% in the 600–800 nm wavelength range. This indicates that interlayer enhances the formation and collection of charge carriers, thereby improving J_{sc}.[64,65] The current density obtained from integrated J_{sc} closely matches the values derived from J–V measurements, affirming device accuracy.

To validate furthermore, stability measurements were carried out in an ambient environment maintained at 25 °C with 35% humidity, as presented in Fig. 7(a) for both base and **NB20** passivated PSCs. After 1000 hours of storage, the **NB20** device was able to maintain >80% of its initial PCE, while the device without **NB20** retained only <59% of its initial PCE value. This clearly indicates that **NB20** imparts significantly enhanced moisture resistance compared to the base device.[66] The improved ambient stability is further supported by water contact angle measurements that assess the influence of the **NB20** impact on the hydrophobicity of the perovskite surface. As shown in Fig. 7(b) and (c), the contact angle increased from 48.2° for the base perovskite film to 81.4° after introducing the **NB20** interlayer. This substantial shift in surface wettability is attributed to the fact that **NB20** exhibits a columnar mesophase at room temperature, driven by strong π–π stacking and ordered molecular alignment resulting from its planar naphthalene-bis(benzimidazole) core and long alkyl chains. Specifically, the branched alkoxy chains in **NB20** enhance the hydrophobicity of the surface, directly increasing the water contact angle. Due to its self-assembling nature, **NB20** forms a thin hydrophobic interfacial layer on the perovskite surface.[12,67–69] This layer reduces the hydrophilicity of the surface, preventing water molecules from diffusing into the perovskite. The hydrophobic groups in **NB20** repel water molecules, reducing the chances of water-induced degradation and thereby enhancing

the device operational stability.[70,71] Thus, the overall stability enhancement observed in the **NB20** based device can be ascribed to a dual mechanism. First, the **NB20** interlayer optimizes interfacial energetics, facilitating efficient charge extraction and suppressing interfacial recombination. Second, its dense and hydrophobic nature acts as an effective barrier against moisture and oxygen penetration, thereby protecting the perovskite layer from environmental degradation. This synergistic behaviour imparts superior moisture resistance and long-term operational stability, confirming the pivotal role of the **NB20** passivation layer in improving device durability and longevity.

Conclusion

The addition of **NB20** at an optimal concentration leads to significant improvements in efficiency and stability within PSCs. At its optimal concentration, charge transport within the device is enhanced, resulting in a PCE of 19.02%. This improvement is due to the ability of **NB20** to passivate surface defects and optimize energy alignment between the absorber layer and HTL, reducing recombination losses and enabling more efficient charge extraction. The increased charge mobility further contributes to the enhancement in performance. Additionally, the stability of solar cells is notably improved with the inclusion of **NB20**. Devices with this concentration exhibit enhanced resilience to environmental conditions, retaining ∼80.69% of their initial efficiency over 1000 hours of storage. This suggests that **NB20** helps reduce perovskite degradation, likely through better passivation of surface defects and minimizing moisture ingress.

Conflicts of interest

There are no conflicts to declare.

Data availability

The data that support the findings of this study are available in the supplementary information (SI) of this article. The SI includes X-ray diffraction (XRD) analysis, time-resolved photoluminescence (TRPL) spectra, current density–voltage (J–V) characteristics, histogram analysis of device performance, electrochemical impedance spectroscopy (EIS) data, and details on the fabrication of space-charge-limited current (SCLC) devices for mobility and trap density analysis. See DOI: https://doi.org/10.1039/d5tc03553h.

Acknowledgements

References

1 S. Bello, A. Urwick, F. Bastianini, A. J. Nedoma and A. Dunbar, *Energy Rep.*, 2022, **8**, 89–106.

2 S. Patwardhan, D. H. Cao, S. Hatch, O. K. Farha, J. T. Hupp, M. G. Kanatzidis and G. C. Schatz, *J. Phys. Chem. Lett.*, 2015, **6**, 251–255.

3 NREL, Cell Efficiency Data Emerging PV, https://www.nrel.gov/images/libraries/pv-images/cellpveffemergingpv.webp?Status=Master&sfvrsn=861cda78_8 (Last accessed: January 28, 2026). There is no corresponding record for this reference.

4 J. Zhuang, J. Wang and F. Yan, *Nano-micro Lett.*, 2023, **15**, 84.

5 J. Manit, P. Kanjanaboos, P. Naweephattana, A. Naikaew, L. Srathongsian, C. Seriwattanachai, R. Supruangnet, H. Nakajima, U. Eiamprasert and S. Kiatisevi, *Sci. Rep.*, 2024, **14**, 1–13.

6 S. Li, Y. Wu, C. Zhang, Y. Liu, Q. Sun, Y. Cui, S. F. Liu and Y. Hao, *ACS Appl. Mater. Interfaces*, 2020, **12**, 45073–45082.

7 W. Li, W. Zhao, K. Li and X. Han, *J. Mater. Chem. C*, 2024, **12**, 1147–1176.

8 L. Nakka, Y. Cheng, A. G. Aberle and F. Lin, *Adv. Energy Sustain. Res.*, 2022, **3**, 2200045.

9 S. Lammar, W. Van Gompel, S. Lenaers, M. Mertens, H. G. Boyen, D. Desta, A. Hadipour, L. Lutsen, D. Vanderzande, A. Krishna, Y. Abdulraheem, T. Aernouts and J. Poortmans, *J. Mater. Chem. C*, 2022, **11**, 8146–8153.

10 A. K. Jena, Y. Numata, M. Ikegami and T. Miyasaka, *J. Mater. Chem. A*, 2018, **6**, 2219–2230.

11 D. Y. Heo, W. J. Jang and S. Y. Kim, *Mater. Today Chem.*, 2022, **26**, 101224.

12 P. K. Behera, K. Yadav, D. S. S. Rao, U. K. Pandey and A. A. Sudhakar, *ACS Appl. Electron. Mater.*, 2023, **5**, 5417–5421.

13 X. Ji, K. Feng, S. Ma, J. Wang, Q. Liao, Z. Wang, B. Li, J. Huang, H. Sun, K. Wang and X. Guo, *ACS Nano*, 2022, **16**, 11902–11911.

14 Z. Kadi, R. Wang, N. Berton, M. Kobeissi, Y. Jiang, J. Gao and B. Schmaltz, *J. Mater. Chem. C*, 2022, **10**, 7680–7689.

15 M. Más-Montoya and R. A. J. Janssen, *Adv. Funct. Mater.*, 2017, **27**, 1605779.

16 E. M. García-Frutos, U. K. Pandey, R. Termine, A. Omenat, J. Barberá, J. L. Serrano, A. Golemme and B. Gómez-Lor, *Angew. Chem.*, 2011, **123**, 7537–7540.

17 K. Yadav, P. Kumar Behera, Ankita, Tarun, R. D. Chavan, P. Yadav, A. Ammathnadu Sudhakar and U. K. Pandey, *Sol. Energy*, 2024, **278**, 112762.

18 F. Zu, M. Roß, L. Frohloff, D. Shin, N. Tessler, S. Albrecht and N. Koch, *Sol. RRL*, 2022, **6**, 2101065.

19 Y. Boeije, W. T. M. Van Gompel, Y. Zhang, P. Ghosh, S. J. Zelewski, A. Maufort, B. Roose, Z. Y. Ooi, R. Chowdhury, I. Devroey, S. Lenaers, A. Tew, L. Dai, K. Dey, H. Salway, R. H. Friend, H. Sirringhaus, L. Lutsen, D. Vanderzande, A. Rao and S. D. Stranks, *J. Am. Chem. Soc.*, 2023, **145**, 21330–21343.

20 R. Tran, X. G. Li, J. H. Montoya, D. Winston, K. A. Persson and S. P. Ong, *Surf. Sci.*, 2019, **687**, 48–55.

21 M. G. Helander, M. T. Greiner, Z. B. Wang, W. M. Tang and Z. H. Lu, *J. Vac. Sci. Technol., A*, 2011, **A29**, 011019.

22 N. Yukta, R. D. Chavan, A. Mahapatra, D. Prochowicz, P. Yadav, P. K. Iyer and S. Satapathi, *ACS Appl. Mater. Interfaces*, 2023, **15**, 53351–53361.

23 J. Dong, D. Song, J. Meng, Y. Lu, Y. Li, B. Qiao, S. Zhao and Z. Xu, *J. Mater. Chem. C*, 2020, **8**, 6743–6748.

24 C. Peng, X. Xia, X. Wang, J. Peng, Z. Fan and F. Li.

25 Y. Wu, H. Zhu, B.-B. Yu, S. Akin, Y. Liu, Z. Shen, L. Pan and H. Cai, *Chem. Eng. J.*, 2022, **433**, 134613.

26 Z. Dai, Z. Yang, X. Huang, S. Wan, L. Yuan, H. Wei, S. Nie, Z. Liu, Y. Wu, R. Chen and H. Wang, *Nano Energy*, 2024, **131**, 110190.

27 H. Lu, A. Krishna, S. M. Zakeeruddin, M. Gratzel and A. Hagfeldt, *iScience*, 2020, **23**, 10135.

28 A. Siddiqui, F. Sadegh, K. Phani Kumar, R. Priksha, P. Yadav, D. Prochowicz, S. P. Singh and S. Akin, *ACS Appl. Mater. Interfaces*, 2024, **16**(13), 16213–16223.

29 N. Guan, Y. Zhang, W. Chen, Z. Jiang, L. Gu, R. Zhu, D. Yadav, D. Li, B. Xu, L. Cao, X. Gao, Y. Chen and L. Song, *Adv. Sci.*, 2023, **10**, 1–10.

30 M. Nukunudompanich, G. Budiutama, K. Suzuki, K. Hasegawa and M. Ihara, *CrystEngComm*, 2020, **22**, 2718–2727.

31 D. He, X. Xu, Z. Liang, Y. Niu, Y. Sun, T. Gavin, P. Falaras and L. Hu, *J. Mater. Chem. C*, 2021, **9**, 9584–9591.

32 D. Kim, K. Higgins and M. Ahmadi, *Matter*, 2021, **4**, 1442–1445.

33 D. H. Kim, C. P. Muzzillo, J. Tong, A. F. Palmstrom, B. W. Larson, C. Choi, S. P. Harvey, S. Glynn, J. B. Whitaker, F. Zhang, Z. Li, H. Lu, M. F. A. M. van Hest, J. J. Berry, L. M. Mansfield, Y. Huang, Y. Yan and K. Zhu, *Joule*, 2019, **3**, 1734–1745.

34 C. Tian, Y. Zhao, X. Han, B. Li, Y. Rui, H. Xiong, Y. Qiu, W. An, K. Li and C. Hou, *Chem. Eng. J.*, 2023, **452**, 139345.

35 S. Li, Y. Wu, C. Zhang, Y. Liu, Q. Sun, Y. Cui, S. F. Liu and Y. Hao, *ACS Appl. Mater. Interfaces*, 2020, **12**, 45073–45082.

36 Y. Li, E. L. Lim, H. Xie, J. Song, T. Kong, Y. Zhang, M. Yang, B. Wu, C. Duan and D. Bi, *ACS Photonics*, 2021, **8**, 3185–3192.

37 R. Li, P. Wang, B. Chen, X. Cui, Y. Ding, Y. Li, D. Zhang, Y. Zhao and X. Zhang, *ACS Energy Lett.*, 2020, **5**(1), 79–86.

38 Q. Jiang, Y. Zhao, X. Zhang, X. Yang, Y. Chen, Z. Chu, Q. Ye, X. Li, Z. Yin and J. You, *Nat. Photonics*, 2019, **13**, 460–466.

39 Z. Li, Y. Xiang, J. Li, L. Feng, M. Zhang, Z. Zhang, S. Yan and B. Xu, *Angew. Chem., Int. Ed.*, 2025, **64**, e202413986.

40 Q. Zhao and F. He, *J. Energy Chem.*, 2024, **93**, 174–192.

41 K. Ye, B. Zhao, B. T. Diroll, J. Ravichandran and R. Jaramillo, *Faraday Discuss.*, 2022, **239**, 146–159.

42 J. Jiang, X. Sun, X. Chen, B. Wang, Z. Chen, Y. Hu, Y. Guo, L. Zhang, Y. Ma, L. Gao, F. Zheng, L. Jin, M. Chen, Z. Ma, Y. Zhou, N. P. Padture, K. Beach, H. Terrones, Y. Shi, D. Gall, T. M. Lu, E. Wertz, J. Feng and J. Shi, *Nat. Commun.*, 2019, **10**, 1–12.

43 Y. Rui, T. Li, B. Li, Y. Wang and P. Müller-Buschbaum, *J. Mater. Chem. C*, 2022, **10**, 12392–12401.

44 M. Z. Tun, P. Pansa-Ngat, P. Ruankham, K. K. Shin Thant, S. Kamnoedmanee, C. Seriwattanachai, W. Rueangsawang, R. Supruangnet, H. Nakajima and P. Kanjanaboos, *Sci. Rep.*, 2023, **13**, 1–12.

45 X. Sun, L. Li, S. Shen and F. Wang, *Nanomaterials*, 2023, **13**(2), 249.

46 A. Ummadisingu and M. Grätzel, *Sci. Adv.*, 2018, **4**, 1–9.

47 N. Marinova, W. Tress, R. Humphry-Baker, M. I. Dar, V. Bojinov, S. M. Zakeeruddin, M. K. Nazeeruddin and M. Grätzel, *ACS Nano*, 2015, **9**, 4200–4209.

48 M. Yuan, H. Ma, Q. Dong, X. Wang, L. Zhang, Y. Yin, Z. Ying, J. Guo, W. Shang and J. Zhang, *Nano Energy*, 2024, **121**, 109192.

49 V. M. Le Corre, J. Diekmann, F. Pena-Camargo, J. Thiesbrummel, N. Tokmoldin, E. Gutierrez-Partida, K. P. Peters, L. Perdigón-Toro, M. H. Futscher and F. Lang, *Sol. RRL*, 2022, **6**, 2100772.

50 R. Zhang, M. Li, Z. Liang, Y. Tang, C. Han, X. Chen, Y. Wang, Y. Yu, S. Liu, L. Xu, R. Chen and W. Lv, *J. Phys. Chem. C*, 2023, **127**, 14098–14106.

51 S. Akin, N. Arora, S. M. Zakeeruddin, M. Grätzel, R. H. Friend and M. I. Dar, *Adv. Energy Mater.*, 2020, **10**, 1903090.

52 Yukta, R. D. Chavan, A. Mahapatra, D. Prochowicz, P. Yadav, P. K. Iyer and S. Satapathi, *ACS Appl. Mater. Interfaces*, 2023, **15**(46), 53351–53361.

53 S. Rahmany and L. Etgar, *Mater. Adv.*, 2021, **2**, 2617–2625.

54 Y. Yun, Q. Chang, J. Yan, Y. Tian, S. Jiang, W. Wei, S. Li, Y. Guo, J. Yin, J. Li, M. Chen, K. Huang, C. Li and R. Zhang, *Sci. Adv.*, 2025, **11**, eadp3112.

55 N. Tzoganakis, B. Feng, M. Loizos, M. Krassas, D. Tsikritzis, X. Zhuang and E. Kymakis, *J. Mater. Chem. C*, 2021, **9**, 14709–14719.

56 E. Jokar, H.-S. Chuang, C.-H. Kuan, H.-P. Wu, C.-H. Hou, J.-J. Shyue and E. Wei-Guang Diau, *J. Phys. Chem. Lett.*, 2021, **12**, 10106–10111.

57 V. M. Le Corre, E. A. Duijnstee, O. El Tambouli, J. M. Ball, H. J. Snaith, J. Lim and L. J. A. Koster, *ACS Energy Lett.*, 2021, **6**, 1087–1094.

58 R. De, J. De, S. P. Gupta, I. Bala, N. Ankita, N. Tarun, U. K. Pandey and S. K. Pal, *J. Mater. Chem. C*, 2022, **11**, 980–985.

59 M. T. Khan, N. H. Hemasiri, S. Kazim and S. Ahmad, *Sustain. Energy Fuels*, 2021, **5**, 6352–6360.

60 H. Sharma, A. Ankita, P. Bhardwaj, U. K. Pandey and S. Das, *Org. Mater.*, 2023, **5**, 72–83.

61 J. Siekmann, S. Ravishankar and T. Kirchartz, *ACS Energy Lett.*, 2021, **6**, 3244–3251.

62 S. Mohammadi, S. A. Nia and D. Abbaszadeh, *Sci. Rep.*, 2024, **14**, 24254.

63 Y. Xu, Q. Niu, Z. Zhang, Z. Zhang, S. Fu, L. Zhang, W. Zeng, A. V. Andrianov, R. Xia and Y. Min, *Org. Electron.*, 2023, **113**, 106692.

64 A. Zare Bidaki, H. Abdizadeh, E. Pourshaban, M. S. Shadabroo and M. R. Golobostanfard, *Mater. Sci. Semicond. Process.*, 2022, **138**, 106259.

65 T. Ohsawa, N. Shibayama, N. Nakamura, S. Tamura, A. Hayakawa, Y. Murayama, K. Makisumi, M. Kitahara, M. Takayama and T. Matsui, *J. Mater. Chem. A*, 2024, **12**, 22510–22515.

66 T. A. Chowdhury, M. A. Bin Zafar, M. Sajjad-Ul Islam, M. Shahinuzzaman, M. A. Islam and M. U. Khandaker, *RSC Adv.*, 2023, **13**, 1787–1810.

67 X. Ye, H. Cai, Q. Sun, T. Xu, J. Ni, J. Li and J. Zhang, *Org. Electron.*, 2022, **106**, 106542.

68 P. Zhao, J. Subbiah, B. Zhang, J. A. Hutchison, G. Ahluwalia, V. Mitchell, K. P. Ghiggino and D. J. Jones, *Adv. Mater. Interfaces*, 2023, **10**, 2202313.

69 W. Chen, V. Karde, T. N. H. Cheng, S. S. Ramli and J. Y. Y. Heng, *Front. Chem. Sci. Eng.*, 2021, **15**, 90–98.

70 Y. Wang, S.-C. Chen, S. Tai, D. Wang, Y. Ma, J. Wu and M.-J. Lin, *J. Mater. Chem. C*, 2024, **12**, 6540–6547.

71 C. Lee, J. Lee, S. Lee, W. Lee, H. You, H. Y. Woo and B. J. Kim, *J. Mater. Chem. A*, 2020, **8**, 3735–3745.